NIST Advanced Manufacturing Series
NIST AMS 100-54

Process-Structure-Property Data Alignment for Additive Manufacturing Data Registration

Shaw C. Feng
Yan Lu
Albert T. Jones

NIST | NATIONAL INSTITUTE OF
STANDARDS AND TECHNOLOGY
U.S. DEPARTMENT OF COMMERCE

Process-Structure-Property Data Alignment for Additive Manufacturing Data Registration

Shaw C. Feng
Yan Lu
Albert T. Jones
Systems Integration Division
Engineering Laboratory

July 2023

NIST AMS 100-54
July 2023

Certain commercial entities, equipment, or materials may be identified in this document in order to describe an experimental procedure or concept adequately. Such identification is not intended to imply recommendation or endorsement by the National Institute of Standards and Technology, nor is it intended to imply that the entities, materials, or equipment are necessarily the best available for the purpose.

NIST Technical Series Policies
[Copyright, Fair Use, and Licensing Statements](#)
[NIST Technical Series Publication Identifier Syntax](#)

Publication History
Approved by the NIST Editorial Review Board on 2023-02-02

NIST Author ORCID iDs
Shaw C. Feng: 0000-0003-1133-6223
Yan Lu: 0000-0003-2927-5860

Contact Information
shaw.feng@nist.gov

Abstract

Melt-pool-monitoring, layer-wise-imaging, microstructure-analysis, and mechanical-property test data are increasingly becoming available during the additive manufacturing (AM) fabrication processes. Combining these data for data analytics is becoming more important because the process-structure-property relationships are needed to monitor AM processes, validate part quality, and improve the qualification process. A major challenge to correlating or fusing these multi-modal data sets is the lack of systematic data alignment methods, because data are obtained at various scales and sampling rates from different sensors, instruments, and testing machines that have their own local coordinate systems. Additionally, these datasets must also be aligned with other build data such as process parameters and scan paths for process planning and control. This paper presents an innovative data-registration method to align AM data acquired through the part development lifecycle, which is the first step towards addressing the correlation and data fusion problem. This method includes the definitions of various reference frames for the aforementioned AM data sets and a common reference, coordinate system, as well as the techniques to transform data between coordinate systems that provide an effective way to use those datasets as inputs to downstream applications such as simulation, machine learning, and data analytics.

Keywords

Contents

List of Figures

1. Introduction

In Additive Manufacturing (AM), the <u>properties</u> of the final AM part heavily depend on as-built material <u>structure</u> formed during the layer-by-layer, fabrication <u>process.</u> Existing research efforts [1, 2, 3] focus on 1) understanding the relationships among the **p**rocess, the **s**tructure, and the **p**roperties (PSP) and 2) using those relationships to improve both the process control and the part quality. Those relationships are material specific and geometry dependent. Understanding these relationships and their impacts on AM process control and the part requires registering the different datasets associated with both material type and geometry features. Registering those datasets involves aligning them temporally and spatially and recording the metadata needed to describe each dataset. Data alignment is a process that involves 1) identifying individual, sensor, measurement, reference frames and 2) transforming each individual one into a common reference frame. The metadata that describes each sensor measurement is also needed to provide the context of the data.

Our earlier research focused on in-situ monitoring data analytics tools. That research includes 1) aligning multi-modal in-situ monitoring data into a common reference coordinate system [4, 5] and 2) creating the metadata that provides the needed context about the relationships among each sensor and each data type [6]. However, those research results cannot be directly applied to registration of a variety of structure and microstructure measurement methods including Scanning Electron Microscopy (SEM), Electron Backscattering Diffraction (EBSD) SEM, Energy Dispersive Scattering (EDS), and X-ray Diffraction Spectroscopy (XDS), as well as mechanical property testing data. These methods and their data outputs can be used to study the microstructure, residual stress, grain structure, mechanical, electrical, magnetic, and thermal properties of AM-built parts. A systematic organization of these properties is needed to be used as feedback to control the fabrication processes and to improve the final, part quality. For example, controlling AM processes for an equiaxed grain structure can improve component quality [7]. Utilizing microstructure data and mechanical test data has the potential to 1) accelerate both material and part qualification processes and 2) reduce the need for additional AM builds and test specimens [8].

In this paper, we focus on three types of Laser-based Powder Bed Fusion of Metals (PBF-LB/M) data [9]: process data, microstructure data, and tensile data. We chose these three types of data because they provide the critical inputs needed to further analyze the PSP relationships. Before performing this analysis, however, it is important to align these three data types. The resulting alignment can be used to better understand the relationships between microstructural morphology with phase composition and mechanical properties. Such an understanding is needed to control the process and qualify the fabricated parts. Today, aligning those data types is still an unsolved research problem.

The main contribution of this paper is a data registration procedure and data alignment methods, which can solve the data registration problems on process, structure, and property datasets. Section 2 reviews currently available research results that correlate AM process data, microstructural data, and property data. Needs and gaps in data registration are identified. Section 3 describes the common coordinate system used for AM data alignment and registration. Section 4 proposes a data alignment method for microstructural data. Section 5 proposes a data alignment method for tensile test data. Section 6 presents the techniques to identify the

transformations necessary for the aforementioned data alignments. Section 7 discusses the methods from the application point of view. Section 8 concludes the methods and briefly discusses possible future work.

2. Current State of AM Process-Structure-Property Data

This section reviews currently available research results that correlate microstructure images with PBF/LB-M process parameters and mechanical properties. Potential gaps identified in this section should be addressed to develop a formal methodology and data infrastructure to relate data from different in-situ monitoring sensors, EBSD SEMs, coordinate metrology instruments, and testing machines.

2.1. Review of Research on Microstructure and Tensile Test Data Correlations

As noted above, there is a critical need to align and correlate microstructure data with in-situ data to analyze the causes and the consequences of part quality problems [10]. Sames et al. [11] correlated microstructural features including defects, pores, and cracks to the scanning strategies in the AM process. Francois et al. [12] modeled the grain-growth direction and melt-pool heating and cooling to show that grain orientation and size are related to the melt-pool moving direction. King et al. [13] proposed simulation models to show the PSP relationships. The authors argued that estimating experimental correlations using measurements of physical phenomena is difficult. More correlations among melt pool, microstructure, residual stress, and mechanical property are discussed as follows.

2.1.1. Melt Pool Image and Microstructure Data Correlation

Recently, many research results about melt-pool solidification and microstructural evolutions in AM have become available. Lee et al [14] described the effects of melt-pool flow on the temperature gradient and solidification rate, both of which impact the crystal growth, size, and orientation in grains. They showed that the melt pool, travel direction, and heat gradient determine the formation of columnar and cellular grains. Chadwick et al. [15] showed a simulation of nucleation and grain growth in the temperature gradient driven by the moving laser beam based on a Rosenthal model. Zhang et al. [16] used a different technique to study impacts of the melt pool, temperature distribution, cooling rate on the part's microstructural evolution. The results showed the impacts of the relative positions and orientations of grain structures on the melt pool and its moving direction. A report from Argonne National Laboratory [17] describes the relationships between the Metal Additive Manufacturing (MAM) process parameters and the part's microstructure. Using modeling and simulation to predict both the initial microstructure and geometric relationships of melt pool and their evolution were reported in [18].

Several studies have addressed the correlations among P(micro)SP relationships for laser-based MAM. For example, Gu et al. [19] reviewed recent work on powder melting, microstructural evolution, grain structures, and mechanical properties of AM parts. Specifically, Gu et al. [20] studied microstructures within the LPBF melt pool where the grain-growth direction, grain size, and grain shape are shown relative to the scan direction and build direction. Additionally,

cellular dendrite, columnar dendrite, and equiaxed grain are predicted in the cross-section and the longitudinal cross-section of the melt pool.

Sahoo et al. [21] proposed a model to simulate the melt-pool's thermal profile in the scan direction. There were two purposes. The first was to correlate the phase profile of the metal at different solidification times. The second was to predict grain growth including the growth rate and microstructure evolution during the solidification process. Zinoviev et al. [22] used a Goldak, double ellipsoid in a local, coordinate system to define the melt-pool shape including its dimensions and moving direction. The authors simulated and measured the grain structures from the polycrystalline substrate. The substrate, melt pool, and crystal orientation needed to be correlated, but only a few details were available. Knapp et al. [23] simulated the melt-pool geometry and graphically overlaid it on optical images of columnar grains. The simulation results allowed researchers to compare the melt-pool's grain-growth direction to its evolving solidification. The comparison was made in both the cross-section of and perpendicular to the moving direction.

Shi et al. [24] reported correlation of the microstructural evolution to both the melt-pool shape and the laser-beam shape. The purpose was to control grain growth and use the results to optimize the mechanical properties. Their results showed that the melt-pool temperature, size, and shape are closely related to the part's microstructure in the traversal, longitudinal, and horizontal directions relative to the melt-pool shape and laser-moving direction. Kelly et al. [25] related the macrostructure and microstructure in a laser-deposited AM part relative to the process parameters, the part's layer thickness, and the laser-beam's dimensions. The microstructures were observed using an optical microscope; however, the image coordinate system and the microscope coordinate system were not explicitly correlated.

Gu et al. [26] studied the effects of the energy density and scanning speed of the laser on the microstructure and the porosity when melting stainless-steel powders. The build direction, laser scanning path, and energy-density readings were defined on the build-plate coordinate system. The microstructure images, however, were based on the local, SEM, coordinate system. The observed pores, unmelted powders, and contaminates on the SEM images were qualitatively related to the energy density readings in the build-plate coordinate system.

2.1.2. Laser-beam Scanning and Microstructure Data Correlation

Stoudt et al. [27] used the build platform coordinate system (CS) to align the microstructural-data CS with the process-data CS. The authors oriented a set of EBSD SEM and EDS images of the test part to study the grain structures. Different images were needed because of the different temperature gradients and cooling rates that occurred during the process. Zitelli et al. [28] reviewed the microstructures and process-related defects of stainless steel parts fabricated during an LPBF process. Micrographs using an optical microscope revealed the microstructure of the samples fabricated in the build direction. These microstructures can be compared with parts fabricated using different, laser-scanning strategies. Different samples are then put under tensile tests, which showed different mechanical properties.

Pham et al. [29] reported the role of grain structure evolution in the solidification process in powder bed fusion. The direction and length of the side-branching showed grain shapes and sizes. The authors aligned side-branching directions with respect to the build direction in the Z axis and laser-beam scanning direction. Their investigation showed that different, layer-by-layer,

scanning strategies can greatly influence the side branching and, thus, can alter the microstructure of an AM fabricated part. Koepf et al. [30] described a method to correlate microstructure with scanning strategies. Grain-growth directions on individual layers were correlated using a melting and remelting simulation. Arisoy et al. [31] used a best-fit algorithm, which correlated melt pool and grain structure to process parameters and scan strategy.

Chen et al. [32] compared a phase-field method with real-time observations using synchrotron X-ray radiography. In their study, the authors used a graph-based technique to correlate grain growth direction, shape, and size with the melt-pool shape, cooling direction, and thermal gradients. Watring et al. [33] introduced the effects of build orientation coupled with laser-energy density on the microstructure and mechanical properties of Inconel 718 parts fabricated using an LPBF process. The build directions of different coupons were correlated with the lack-of-fusion defects in the coupons, the crystal structures, and the mechanical properties.

Hanzl et al. [34] investigated the influence of process parameters on the mechanical properties of LBPF- built, AM parts. The authors described the part's orientation relative to the build-plate orientation, melting directions, and scanning direction to the mechanical properties including tensile strengths and elongations. Benzing et al. [35] tracked defects and microstructural heterogeneities in tensile coupons. The authors (1) correlated the coupon orientation relative to the build plate coordinate system, (2) located the defects observed in images of the fracture surface, and (3) correlated fracture and microstructure to the scanning and melting during processing.

2.1.3. Melt Pool and Fracture Data Correlation

Qiu et al. [36] described the melt-pool's role in influencing the porosity development in the LPBF process. For example, the authors used SEM images to identify pores that had their own, local CS. The melt-pool, however, was in another local CS. The authors correlated the two coordinate systems using melt-pool images, which were taken with a high-speed camera, as inputs to a thermal, fluid-flow simulation. Those images were in the same CS as the camera CS. Vastola et al. [37] developed a model to predict keyholing effects that could be related to microstructures.

Zheng et al. [38] developed a method to predict porosity formation based on the moving melt pool during the scan in LPBF. The authors correlated an SEM image of the part's microstructure with the simulated melt-pool geometry. The purpose was to study the formation of different microstructures based on the different energy densities associated with the laser power and scan speed. Kruth et al. [39] conducted experiments to better understand the influence of scanning strategies on the microstructural evolution and the subsequent impacts on the mechanical properties of the coupons.

Bartlett et al. [40] measured the residual stresses and correlated it with process variables including layer thickness, part stiffness, and base stiffness in an experiment. Scanning paths were correlated with the estimated, in-plane, residual stress of each layer. The work showed mechanical property and scanning paths alignment possible and could generate useful information. Bauereiss et al. [41] observed defect formation and propagation during a PBF/LB-M process. The melt pool was observed in the build-plate CS; but defect formation and propagation were observed in the microscope's local CS. Since the part's pores and crack development and the melt-pool, moving direction were in two separate CSs, the authors

graphically overlaid them, i.e., manual alignment. Lewandowski et al. [42] reviewed tensile and hardness tests on many coupons that were built in different orientations. They concluded from their tests that microstructures, fractures, and properties could be aligned for cause-and-effect analyses.

2.2.   Gaps in Process, Microstructure, and Property Data Correlations

From the previous literature review, the process data, microstructure data, and mechanical-property data were primarily overlaid graphically using the build plate coordinate system. Studies that focus on nominal process parameters, average microstructure properties, and mechanical tests can simply use a common, reference frame as the center for aligning related data. Melt pool, scanned track, coupon[1], sample[2], specimen[3], and fracture are not well aligned geometrically. As a result, tracing sample defects to process parameters (such as laser power, scan speed, scan pattern, and layer thickness) is difficult. Specifically, we identified the following four barriers when correlating data.

(1) Few standardized CS transformations for both in-situ and ex-situ measurements, for example, melt pool geometry and other local CSs are not well correlated to the build platform CS.

(2) Little standard practice on data alignment to enable efficient data correlation for AM, for example, the test-coupon CS cannot be correlated with the build platform CS.

(3) Lack of established methods to conduct feature-based alignment using least-square fitting algorithms.

(4) Few methods exist to locate the fracture surface relative to the coupon CS.

A proposed data alignment procedure with methods to remove these barriers is described next.

---

[1] A dog-bone shape fabricated in the same build with the part to represent some properties of the part. One or a set of coupons is used in destructive tests as the surrogate of the AM part.
[2] A selected section of the coupon for microstructural analysis.
[3] A sub area of the sample that is prepared (polished with focused ion beam) for microscopy.

3. Build Plate Coordinate System and Melt Pool Data Alignment

A melt pool is created when the laser beam melts the powders. As shown in Figure 1, the central pixel of the laser spot in the image is used as the reference point when aligning the build platform CS with the melt pool CS. The laser-spot center in the coaxial-camera CS can be estimated using the intensity gradient of the melt pool shown in the image. The laserspot center on the scan path is in the scanning laser CS.
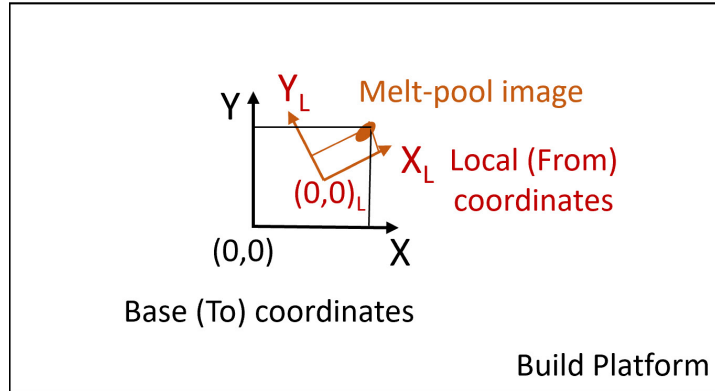
Fig. 1. A melt pool local coordinate system on the build platform.

The relative orientation between the image ("from") and the layer ("To") can be computed using an appropriate, image-calibration method. For example, an image-calibration artifact with black-and-white grids may be used to measure the relative difference between the orientation in the coaxial-camera CS and the orientation in the laser scanning CS. To align the artifact to the build platform, one edge of the black-and-white-grid artifact must be aligned with one edge of the build platform see [3] for more details.

The build platform CS (see Figure 2) can be used as the primary reference CS in the layer-by-layer scanning process [43]. A staring camera is used to take an image of the build platform, The image is on the X-Y plane; and the Z direction, as usual, is perpendicular to the X-Y plane. The Z-X plane can be established by the mid-plane of the front and rear planes. How to detect edges is described below on edge-fitting. For fitting the two edges, both lines must be parallel. The Y-Z plane can be established by the mid-plane of both the left and right planes and must be perpendicular to both X-Y and Z-X planes. The intersection of the three planes is the origin.
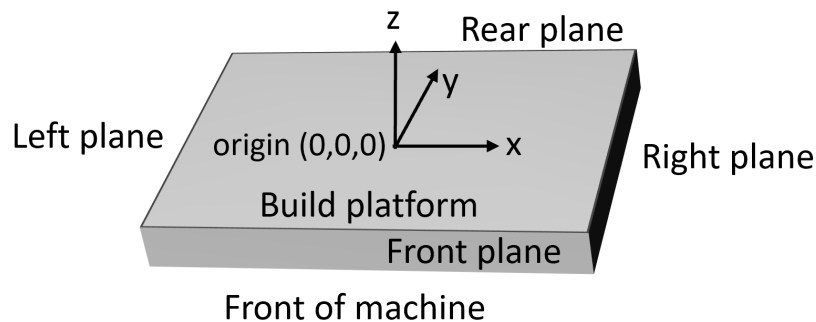
Fig. 2. Build platform coordinate system.

If a rectangular part occupies a small region on the build platform, as shown in the upper right corner of Figure 3, the field of view of the staring camera is only a sub-area of the build platform. Note that the image of the part is distorted due to the camera lens's spherical shape and its sizable thickness. A local CS (X_{local}, Y_{local}) is thus needed. The Laser beam CS denoted as (X_L,Y_L) is on the layer that is parallel to the build platform. The same method as above can be applied. Note that X_L and X_{local} are parallel to each other as is Y_L and Y_{local} since the two CSs are created by the same laser beam. The build platform CS is established from the build-plate shape. The laser CS is established from the build platform CS. Finally, a local CS is established from the laser beam CS.

Types of melt pool-related data in data registration include the dimensions (length, width, and depth), area of the melt pool, thermal gradient, laser spot center location, maximum melt pool temperature, solidification velocity, and melt pool condition (lack-of-fusion, normal, or over-heating/keyholing). These types of data directly affect the microstructure of the fabricated part.

4. Microstructural Data Alignment

A method for establishing a specimen Coordinate System (CS) relative to the Build Plate CS is described in this section, which includes possible microstructural data sources. Then, a method to establish related coordinate systems is introduced.
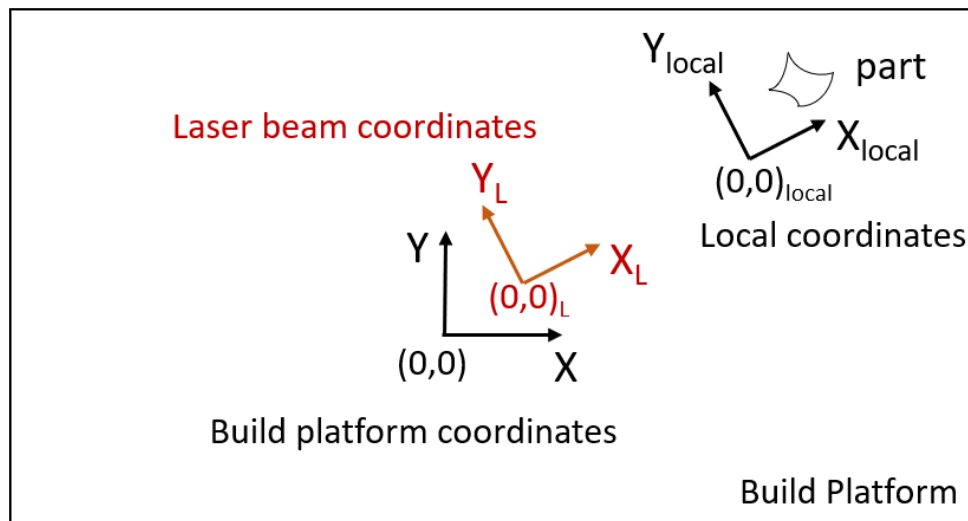
Fig. 3. Staring camera and build platform coordinate systems.

Possible, microstructural, data sources include microscopes and spectroscopes. Optical microscopy (OM) is commonly used in microstructural analysis. OM images can provide information on the melt-pool depth, in both longitudinal and traverse directions, track cross-section, grain morphology, and distribution of porosity. SEM is frequently used to predict some or all primary phases, grain size, aspect ratio, dendritic vs. equiaxed microstructure, and elemental segregation within the thick and thin features of an AM part. These microstructures are impacted by the temperature gradient and cooling rate, which are determined by the melt pool characteristics. SEM images can be observed from either the transverse or longitudinal part views. EBS can provide detailed information on grain size, grain orientation, inclusions, and

defects in grain boundaries. EDS provides elemental analysis of the material in microstructural analysis.

Powder X-Ray Diffraction (PXRD) is used to identify the phases and phase fractions, including the most common precipitates, within the specimens. PXRD allows us to evaluate phase composition, crystallite size, strain, and defects [44]. Ultra-small-angle X-ray scattering (USAXS) instruments provide information about the microstructure of a specimen over a larger length scale that ranges from below one nanometer to multiple micrometers. The pinhole small-angle X-ray scattering (SAXS) technique is used to study the small-length scales in the nanometer range. The wide-angle scattering (X-ray diffraction) technique is used to obtain the phase information, including the most common precipitates. This work focuses only on OM, SEM, and EBSD SEM, but can be later extended to other techniques.

Grain structure analysis can be performed before and after mechanical (for example, tensile and fatigue) testing. SEM images provide information on the microstructural features in fracture, such as pores, cracks, unmelted powders, and soots. In addition, the grain structure including sizes, orientations, and phases can be measured and analyzed using SEM. A coupon is used for destructive evaluation as a surrogate of the part under evaluation. The coupon is fabricated in the Laser CS (X_L, Y_L, Z_L) (see Figure 4). A sample is cut from the coupon. The coupon CS is (X_C, Y_C, Z_C). It is used to reference the sample. After the cut, local sample CS is (X_S, Y_S, Z_S). Images can be taken using a microscope. Since microstructures are very small compared to the average melt pool size, the center of the viewing area can represent the location of the microstructure. The orientation is in the direction of Z_S.

The transformation between sample CS (X_S, Y_S, Z_S) and coupon CS (X_C, Y_C, Z_C), as well as that between coupon CS (X_C, Y_C, Z_C) and laser CS (X_L, Y_L, Z_L) must be obtained first. Then, the location and orientation of the microstructure can be transformed to the Laser CS for relating to melt pools and layers in the build. Hence, issues found from analyzing the images including melting, melt pool formation, cooling, and solidification can then be traced back to the in-process monitoring. In microstructure data registration, the purpose of the microstructural analysis needs to be registered as well. (Note: there are existing international standards [45] that provide methods and procedures to characterize microstructures in metallic materials, including grain sizes and boundaries, textures, phases, voids, and precipitates.) Examples are (1) measurements of features, such as crevices, twins, (average, largest, duplex) grain sizes [46 - 54], and voids [55]; (2) characterizations of grain boundaries, precipitates [56, 57], inclusions, soots, and texture [58]; (3) identifications of phase constituents and their volume fractions in the specimen, and orientation and misorientation relationships between grains and phases; and (4) analysis of fractures. Note that more than one sample should be cut from various locations to represent the global microstructure of a coupon. Figure 4 only shows one specimen as an example.

5. Test Coupon Fracture Coordinate System and Build Plate Coordinate System

This section describes a method for relating both the fractured surface CS to the coupon CS and then the coupon CS to the build plate CS (see Figure 5). The microstructures include pores, ruptures, soots, unmelted powders, and striations. Typically, coupons that are used as tensile-test specimens are fabricated at the same time during the same build. The properties of a coupon are like those of the part. During mechanical testing, specimens are deformed with elongation,

fracture, and distortion. To trace the defects to the process, we need to relate fracture surface and point features on the surface to the original shape. Figure 5 (A) shows a specimen directly fabricated from an AM process, where the specimen is also a coupon, in the CS (X_C, Y_C, Z_C). Because of the deformation, location marks are placed on the coupon. Location marks in the X_C, Y_C, Z_C directions indicate the original X, Y, Z locations in the coupon CS, respectively.

After the coupon is fractured, the fractured portions are elongated because the applied force exceeds the yield strength. The marks preserve the original positions. The fracture surface can then be related to the coupon CS in the X_C direction, as shown in Figure 5 (B). The features on the fractured surface can also be related to the X and Y coordinates (X_C, Y_C) in the coupon CS, as shown in Figure 5 (C).
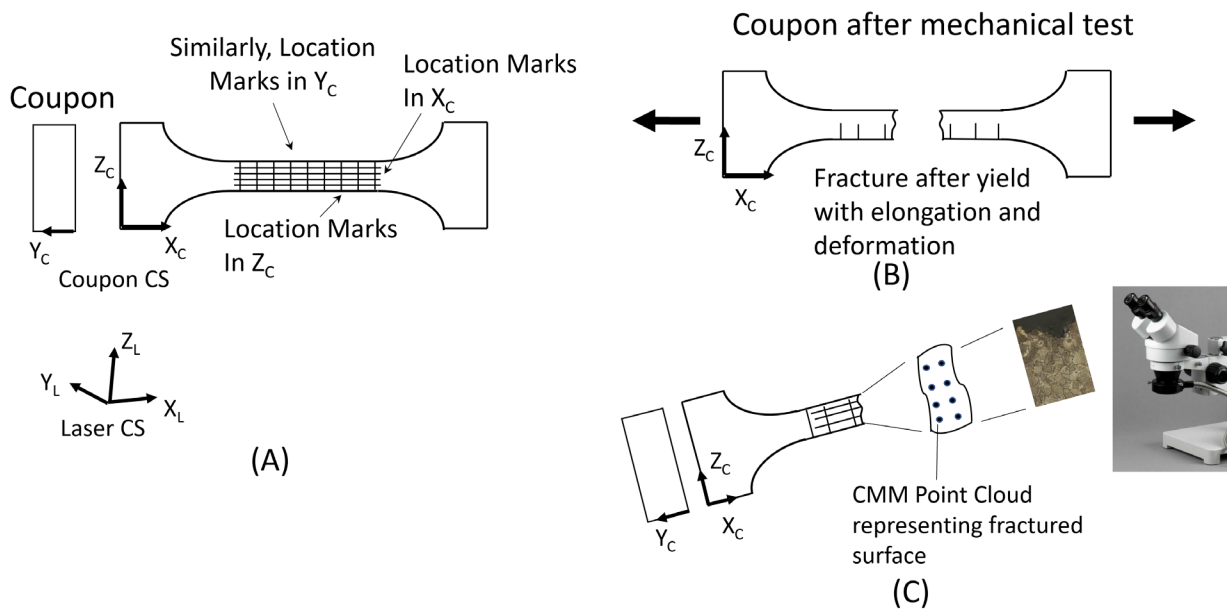
Fig. 4. Property test data coordinate systems.

6. Coordinate System Transformation

The transformation of various coordinate systems within the build chamber is straightforward because all the former reference frames are static. In addition, both the motions of the laser beams and material images are conducted on the build surface. Hence, their coordinate transformations can be simply represented as a matrix operation where the matrix can be obtained through a calibration process. However, registering in-process data with post-process inspection or testing data is relatively complex because tracing the relationships between their related but different coordinate systems is difficult if not impossible. Hence, the required data registration must rely on feature recognition and data alignment only. These features can have fiduciary marks, part-geometry characteristics, structural characteristics, and pore/grain morphologies, for example.

6.1.   In-Process Control Coordinate System Transformation

For laser positioning control, the scan position [x, y] is defined in the build-platform CS, which is shown in Figure 2, to represent any laser beam position on the build surface. However, the galvo command [x_{gcmd}, y_{gcmd}] is defined in the laser-beam CS to set the angle positions of the two mirrors. Assuming the galvo controller is linear, the relationship between these two coordinate systems is a purely 2D geometric transformation including translation and rotation.

$$\begin{pmatrix} x_{gcmd} \\ y_{gcmd} \end{pmatrix} = \begin{bmatrix} \cos{(\theta)} & \sin{(\theta)} \\ -\sin{(\theta)} & \cos{(\theta)} \end{bmatrix} \begin{pmatrix} x - x_0 \\ y - y_0 \end{pmatrix} \tag{1}$$

Where θ is the rotation parameter and x_0 and y_0 are the location of the origin of the galvo command in the build platform coordinate system. The transformation parameters can be identified through calibration [59]. Note, Eq. 1 also applies to the coordinate system transformation between commanded positions and actual positions. The Iterative Closest Point (ICP) registration method [60] is frequently used to identify the translational and rotational parameters in the equation.

6.2.   Co-Axial Melt-Pool-Imaging Coordinate Transformation

Co-axial, melt-pool, imaging systems are set up on the laser optical path, which can generate high-resolution images at high sampling rates, with the melt pool remaining nominally stationary in the field of view. The object plane of the MPM imaging system is focused and occurs on the XY build plane, however, the image orientation does not align with the XY axes [61]. Assuming that the center of the melt pool image is the center of the laser beam, given the laser position when as image is taken [x_{MPM}, y_{MPM}], the pixel resolution and the melt pool image rotation angle, the relationship between the pixel index [x_p^{MPM}, y_p^{MPM}] and the real world position on the build surface [x, y] can be represented:

$$\begin{pmatrix} x \\ y \end{pmatrix} = \begin{bmatrix} \cos{(\theta)} & \sin{(\theta)} \\ -\sin{(\theta)} & \cos{(\theta)} \end{bmatrix} \begin{pmatrix} x_p^{MPM} - x_c^{MPM} \\ y_p^{MPM} - y_c^{MPM} \end{pmatrix} + \begin{pmatrix} x_{MPM} \\ y_{MPM} \end{pmatrix} \tag{2}$$

Where θ is the rotation parameter between melt pool images and the build plane, (x_c^{MPM}, y_c^{MPM}) is the center of the image in pixels in the melt pool imaging coordinate system. The transformation parameters can be identified through calibration [61].

6.3.   Staring Camera Data Registration

Registering image data collected from a starting camera can be done in a variety of ways depending on what metadata and calibration images are available. Registering staring camera images can be done using a series of transformations that map the image coordinates to build-plate coordinates. The transformation can be expressed as a projection from points on the build plate to the image plane. Typically, an explicit, camera-calibration method is used to model the transformation as a pinhole, camera projection from 3D world coordinates [x, y, z] to 2D image coordinates [u, v] [62, 63].

$$s \begin{pmatrix} u \\ v \\ 1 \end{pmatrix} = \begin{pmatrix} f_x & 0 & c_x \\ 0 & f_y & c_y \\ 0 & 0 & 1 \end{pmatrix} \begin{pmatrix} r_{11} & r_{12} & r_{13} & t_1 \\ r_{21} & r_{22} & r_{23} & t_2 \\ r_{31} & r_{32} & r_{33} & t_3 \end{pmatrix} \begin{pmatrix} x \\ y \\ z \\ 1 \end{pmatrix} \qquad (3)$$

The projection matrix is split into intrinsic parameters, as described in the camera matrix A, and extrinsic parameters. Intrinsic parameters are inherent to a camera setup . The intrinsic parameters are described in the camera matrix A and include f_x, f_y, which are projection factors in the u and v axes and the cotangent of a half of the viewing angle. The principal point (c_x, c_y) are the center of the projection. These intrinsic parameters are represented in pixel units. s is the skew coefficient which is non-zero if the image axes are not perpendicular. Extrinsic parameters, which are determined by the camera pose, characterize the rotation and translation of the coordinate plane.

In most situations, the parameters are not known in advance. Consequently, camera calibration must be conducted to retrieve both the intrinsic and extrinsic parameters. Most camera-calibration methods and open-source libraries are designed for 3D systems where either the camera or the object is expected to move in 3D space. As such, the primary goal of most camera-calibration methods is to determine the intrinsic parameters since they can be applied across all camera poses. However, for most LPBF systems, both the camera and the build-plate positions are constant throughout the build. Therefore, an explicit, camera model is not necessary to determine an accurate, global mapping. Instead, a simple Direct Linear Transform (DLT) method can be used to estimate the transformation from a 2D world to a 2D image projection [66]. It is assumed that both reference points and built parts are planar objects flush to the build plate. Hence Eq. 3 can be re-written as Eq. (4).

$$s \begin{pmatrix} u \\ v \\ 1 \end{pmatrix} = \begin{pmatrix} h_{11} & h_{12} & h_{13} \\ h_{21} & h_{22} & h_{23} \\ h_{31} & h_{32} & h_{33} \end{pmatrix} \begin{pmatrix} x \\ y \\ 1 \end{pmatrix} \qquad (4)$$

The h33 value is set to 1 since it is a redundant, scale factor. The least squares method can be used to solve for the 8 degrees of freedom, requiring a minimum of 4 known point correspondences.

6.4. 3D Data Registration

CAD models, XCT data, 3D scan command, 3D scan actual positions, as well as optical serial sectioning data can be sampled to generate 3D point clouds. When scaling or shear mapping distortion is not considered, the relationship between the cloud can be represented as 3D rigid transformation, which is a geometric transformation of a Euclidean space that preserves the Euclidean distance between every pair of points, shown in Eq. 5.

$$\begin{pmatrix} x_2 \\ y_2 \\ z_2 \\ 1 \end{pmatrix} = \begin{pmatrix} i_1 & j_1 & k_1 & t_x \\ i_2 & j_2 & k_2 & t_y \\ i_3 & j_3 & k_3 & t_z \\ 0 & 0 & 0 & 1 \end{pmatrix} \begin{pmatrix} x_1 \\ y_1 \\ z_1 \\ 1 \end{pmatrix} \qquad (5)$$

$$\begin{pmatrix} i_1 & j_1 & k_1 \\ i_2 & j_2 & k_2 \\ i_3 & j_3 & k_3 \end{pmatrix} = \begin{pmatrix} 1 & 0 & 0 \\ 0 & \cos\phi & -\sin\phi \\ 0 & \sin\phi & \cos\phi \end{pmatrix} \begin{pmatrix} \cos\varphi & -\sin\varphi & 0 \\ \sin\varphi & \cos\varphi & 0 \\ 0 & 0 & 1 \end{pmatrix} \begin{pmatrix} \cos\theta & 0 & \sin\theta \\ 0 & 1 & 0 \\ -\sin\theta & 0 & \cos\theta \end{pmatrix} \quad (6)$$

Here $\phi, \theta, and \; \varphi$ are the Euler angles defining the rotation around x, y and z axis, respectively. Vectors i, j, and k are unit vectors of the destination coordinate system.

Again, the global registration, ICP registration, and colored, point-cloud registration methods are the commonly used techniques to identify the transformation between two sets of 3D points. Open3D provides a library to solve the problems. Sometimes, however, engineers need to register a single plane (for example, two-dimensional post-build microscopy) to a 3D data set. To do so, the transformation from Eqs. 5 and 6 are applicable as well and identified using the population-based, heuristic algorithm known as differential evolution (DE) [64].

6.5. Feature Based Registration

The datasets acquired through the AM, part-development lifecycle are multimodal. The main challenge of multimodal registration is to define the right fitness function to optimize the coordinate system transformation. Such a fitness function is needed because different modalities do not exhibit the same characteristics of data. In this case, the part geometry or defect features can be matched and aligned for data registration. Multiple features can be used as references to reduce registration errors. Feature correspondence can be done manually using the techniques shown in Figure 5 or automatically using deep learning techniques.
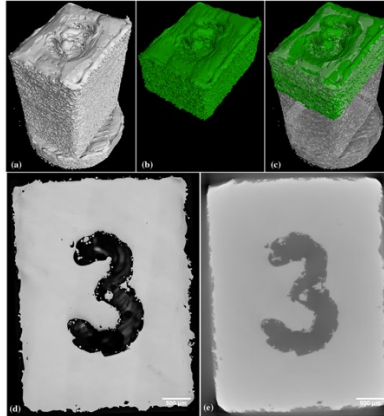
Fig. 5. Feature registration of AM section data with XCT data [65].

For example, fiduciary marks or defects such as pores and cracks in the 3d spaces can be matched using volume registration methods, to create a rigid body transformation. To increase local accuracy, multiple local transformations can be used to reduce the local errors.

7. Discussion

In this paper, we presented methods to align data from various sources - including AM in-process monitoring, ex-situ microstructure inspections, and mechanical tests - to build-platform CS, which is defined in ISO/ASTM 52921. Laser marks are used to identify the origin and

orientation of the laser-beam CS on the build platform CS. The results can create uncertainty due to the variations in the laser power intensity and the galvanometer positioning. These variations can affect the laser-mark, image quality.

For microstructure data alignment, a microscopic image must be first aligned with the sample CS, which is in the build plate CS. To do this, we primarily focused on analyzing SEM images since they can be easily located and oriented relative to the local specimen CS. Other types of data from XRD, EDS, and ultrasmall-, small-, and wide-angle X-ray scattering are more complicated because, as noted above, they range from the nanometer to the micrometer scales. They can be dealt with later when needs are present. SEM specimens for microstructural data analysis are cut and polished [66 - 68]. (Note: there are existing international standards that guide users to prepare specimens of metallic materials.) Because of the precision of the cut, the location and orientation of the specimen relative to the sample CS can be easily measured and reported from the same instrument that is used to prepare the samples and specimens.

Overall, a new data-alignment procedure and its associated alignment methods are proposed. The procedure involves coordinate transformations traceable from mechanical test data to microstructure data to melt pool data. The data are collected from different sensors, microscopic instruments, and tested coupons that live in their local CSs. Then, the local CSs are transformed to the build platform CS. The build platform CS is the commonly referenced CS. With data alignment, features in microstructural data, such as voids, unmelted particles, cracks, inclusions, texture, and grain sizes can be traced to process parameters including melt pool sizes for root cause analysis. Challenges remain in meeting industry needs to use various cases in different materials, process parameters, and design models [6].

8. Conclusions and Future Work

This paper proposes a procedure for aligning microstructural data with both process data and property data. Microstructural images, which are collected using an EBSD-SEM instrument, could be used to predict the mechanical properties of the part. A method to align microstructural data with property data was described. That method uses microstructure images in the specimen local CS, which is in the sample CS. We also proposed a method to relate mechanical property data in the coupon CS to the build plate CS.

In addition, the paper also described a method to align microstructural data with AM process data. Process parameter data, including laser power, beam size, and scanning speed influence microstructure including grain size, grain orientation, and phases are in the build platform CS. The proposed method aligns process data in the built-platform CS to microstructural data in the specimen CS. The test specimens are part of the sample and are placed in the local sample CS. The sample is in the laser CS. The laser CS is related to the build plate CS using two mutually perpendicular, thin-laser marks. To this end, process data, microstructural data, and mechanical property data are all in a common build-platform CS. Grain locations and orientations are thus aligned with process data and property data.

Further research activities are suggested as follows. First, any correlation of the laser CS to the build plate CS should be further investigated using a smaller laser beam to make finer and more precise marks to locate the laser CS on the build plate. Second, we propose setting fiduciary marks in SEM images for the purpose of aligning microstructural data in the sample to microstructural data in the sample CS. Lastly, it is necessary to improve the method to determine

the fracture surface's location and orientation in the coupon so that features shown in the fracture can be better located in the coupon CS.

Disclaimer

Certain commercial equipment, instruments, or materials identified in this paper are not intended to imply recommendation or endorsement by the National Institute of Standards and Technology, nor is it intended to imply that the materials or equipment identified are necessarily the best available for the purpose. Any opinions, findings, conclusions, or recommendations expressed in this material are those of the authors and do not necessarily reflect the views of NIST or any other supporting U.S. government or corporate organizations. Further, this material is declared a work of the U.S. Government and is not subject to copyright protection in the United States of America.

References

[1] NASA / NIST / FAA Technical Interchange Meeting on Computational Materials Approaches for Qualification by Analysis for Aerospace Applications, NASA/TM–20210015175, May 2021.

[2] Department of Defense Additive Manufacturing Roadmap, Final Report, #88ABW-2016-5841, November 2016.

[3] Mani, M., Lane, B., Donmez, A., Feng, S., and Moylan, S., "A Review on Measurement Science Needs for Real-time Control of Additive Manufacturing Metal Powder Bed Fusion Processes," International Journal of Production Research, Volume 55, Issue 5, 2017, pp. 1400-1418.

[4] Feng, S., Lu, Y., and Jones, A. (2020) "Measured data alignments for monitoring metal additive manufacturing processes using laser powder bed fusion methods," Proceedings of ASME 2020 International Design Engineering Technical Conferences and Computers and Information in Engineering Conference, IDETC/CIE 2020-22478.

[5] Lu, Y., Yang, Z., Kim, J., Cho, H., and Ho, Y., "Camera-based Coaxial Melt Pool Monitoring Data Registration For Laser Powder Bed Fusion Additive Manufacturing," Proceedings of the ASME 2020 International Mechanical Engineering Congress and Expo, November 2020, paper #: IMECE2020- 23180.

[6] Feng, S., Lu, Y., and Jones, A. (2020) "Meta-data for in-situ monitoring of laser powder bed fusion processes," Proceedings of ASME 2020 Manufacturing Science and Engineering Conference, MSEC 2020-8344.

[7] Todaro, C., Easton, M., Qiu, D., et al., "Grain structure control during metal 3D printing by high-intensity ultrasound," Nature Communications, 2020, https://www.nature.com/articles/s41467-019-13874-z

[8] Seifi, M., Salem, A., Beuth, J., Harrysson, O., and Lewandowski J., "Overview of materials qualification needs for additive manufacturing," Journal of Materials, Vol. 68, No. 3, 2016, pp. 747 – 764.

[9] ISO/ASTM 52911-1:2019, Additive manufacturing - Design - Part 1: Laser-based powder bed fusion of metals, International Organisation for Standardization, 2019.

[10] Galy, C., Guen, E., Lacoste, E., and Arvieu, C., "Main defects observed in aluminum alloy parts produced by SLM: from causes to consequences," J. Additive Manufacturing, Vol. 22, 2018, pp. 165 – 175.

[11] Sames, W., List, F., Pannala, S., Dehoff, R., and Babu, S., "The metallurgy and processing science of metal additive manufacturing," International Materials Reviews, Vol. 61, No. 5, 2016, pp. 315 – 360.

[12] Francois, M., Sun, A., King, W., et al., "Modeling of additive manufacturing processes for metals: challenges and opportunities," Current Opinion in Solid State and Materials Science, Vol. 21, 2017, pp. 198 – 206.

[13] King, W., Anderson, A., Ferenccz, R., Hodge, N., Kamath, C., Khairallah, S., and Rubenchik, A., "Laser powder bed fusion additive manufacturing of metals; physics, computational, and material challenges," Applied Physics Reviews, Vol. 2, 2015, #041204.

[14] Lee, Y and Zhang, W., "Modeling of heat transfer, fluid flow and solidification microstructure of nickel-based superalloy fabricated by laser powder bed fusion," J. Additive Manufacturing, Vol. 12, 2016, pp. 178 – 188.

[15] Chadwick, A. and Voorhees, P., "The development of grain structure during additive manufacturing," Acta Materialia, Vol. 211, 2021, #116862.

[16] Zhang, Z, Tan, X., Hu, C., Ge, P., Wan, Z., Li, J., and Wu, Q., "Numerical methods for microstructural evolutions in laser additive manufacturing," J. Computers and Mathematics with Applications, Vol. 78, 2019, pp. 2296 – 2307.

[17] Applied Materials Division, "Survey of methods for predicting material performance from material microstructure for advanced manufacturing technologies," Argonne National Laboratory, ANL-20/40, 2020.

[18] Applied Materials Division, "Survey of modeling and simulation techniques for predicting initial microstructures for advanced manufacturing technologies," Argonne National Laboratory, ANL-20/21, 2020.

[19] Gu, D., Meiners, W., Wissenbach, K., and Poprawe, R., "Laser additive manufacturing of metallic components: material, processes and mechanisms," International Materials Reviews, Vol. 57, No. 3, 2012, pp. 133 – 164.

[20] Gu, D., Shi, Q., Lin, K., and Xi, L., "Microstructure and performance and underlying thermal mechanisms of Ni-based parts fabricated by selective laser melting," J. Additive Manufacturing, Vol. 22, 2018, pp. 265 – 278.

[21] Sahoo, S. and Chou, K., "Phase-field simulation of microstructure evolution of Ti-6Al-4V in electron beam additive manufacturing process," J. Additive Manufacturing, Vol. 9, 2016, pp. 14 – 24.

[22] Zinoviev, A., Zinovieva, O., Ploshikhin, V., Romanova, V., and Balokhonov, R., "Evolution of grain structure during laser additive manufacturing simulation by a cellular automata method," J. Materials and Design, Vol. 106, 2016, pp. 321 – 329.

[23] Knapp, G., Raghavan, N., Plotkowski, A., and DevRoy, T., "Experiments and simulations on solidification microstructure for Inconel 718 in powder bed fusion electron beam additive manufacturing," J. Additive Manufacturing, Vol. 25, 2019, pp. 511 – 521.

[24] Shi, R., Khairallah, S., Roehling, T., Heo, T., McKeown, J., and Matthews, M., "Microstructural control in metal laser powder bed fusion additive manufacturing using laser beam shaping stragegy," Acta Materialia, Vol. 184, 2020, pp. 284 – 305.

[25] Kelly, S. and Kampe, S., "Microstructural evolution in laser-deposited multilayer Ti-6Al-4V builds: Part I. Microstructural characterization," Metallurgy and Materials Transaction A, Vol. 35A, 2004, pp. 1861 - 1867.

[26] Gu, H., Gong, H., Pal, D., Rafi, K., Starr, T., and Stucker, B., "Influences of energy density on porosity and microstructure of selective laser melted 17-4PH stainless steel," Proceedings of Solid Freeform Fabrication Symposium, 2013, pp. 474 – 489.

[27] Stoudt, M., Williams, M., Levine, L., Creuziger, A., Young, S., Heigel, J., Lane, B., and Phan, T., "Location-specific microstructure characterization within IN625 additive manufacturing benchmark test artifacts," J. Integrating Materials and Manufacturing Innovation, Vol. 9, 2020, pp. 54 – 69.

[28] Zitelli, C., Folgarait, P., and Di Schino, A., "Laser powder bed fusion of stainless steel grades: a review," J. Metals, Vol. 9, 2019, #731.

[29] Pham, M., Dovgyy, B., Hooper, P., Gourlay, C., and Piglione, A., "The role of side-branching in microstructure development in laser powder-bed fusion," Nature Communications, Vol, 11, 2020, #749.

[30] Koepf, J., Gotterbarm, M., Markl, M., and Koener, C., "3D multi-layer grain structure simulation of powder bed fusion additive manufacturing," Acta Materialia, Vol. 152, 2018, pp. 119 – 126.

[31] Arisoy, Y., Criales, L., Oezel, T., Lane, B., Moylan, S., and Donmez, A., "Influence of scan strategy and process parameters on microstructure and its optimization in additively manufactured nickel ally 625 via laser powder bed fusion," Int. J. Adv Manufacturing Technologies, Vol. 90, 2017, pp. 1393 – 1417.

[32] Chen, Y., Bongo, A., Xiao, N., Billia, B., Kang, X., Nguyen-Thi, H., Luo, X., and Li, D., "Quantitatively comparing phase-field modeling with direct real time observation by synchrotron X-ray radiography of the initial transient during directional solidification of an Al-Cu alloy," Acta Materialia, Vol., 60, 2012, pp. 199 – 207.

[33] Watring, D., Benzing, J., Hrabe, N., and Spear, A., "Effects of laser-energy density and build orientation on the structure-property relationships in as-built Inconel 718 manufactured by laser powder bed fusion," J. Additive Manufacturing, Vol. 36, 2020, pp. 101425.

[34] Hanzl, P., Zetek, M., Baksa, T., and Kroupa, T., "The influence of processing parameters on the mechanical properties of SLM parts," Procedia Engineering, Vol. 100, 2015, pp. 1405 – 113.

[35] Benzing, J., Liew, L., Hrabe, N., and DelRio, F., "Tracking defects and microstructural heterogeneities in meso-scale tensile specimens excised from additively manufactured parts," J. Experimental Mechanics, Vol. 60, 2020, pp. 165 – 170.

[36] Qiu, C., Panwisawas, C., Ward, M., Basoalto, H., Brooks, M., and Attallah, M., "On the role of melt flow into the surface structure and porosity development during selective laser melting," Acta Materialia, Vol. 95, 2015, pp. 72 –79.

[37] Vastola, G., Pei, Q., and Zhang, Y., "Predictive model for porosity in powder-bed fusion additive manufacturing at high beam energy regime," J. Additive Manufacturing, Vol. 22, 2018, pp. 817 – 822.

[38] Zheng, M., Wei, M., Chen, J., Zhong, C., Lin, X., and Huang, W., "A novel method for the molten pool and porosity formation modelling in selective laser melting," Intl. J. Heat and Mass Transfer, Vol. 140, 2019, pp. 1091 – 1105.

[39] Kruth, J., Badrossamay, M., Yasa, E., Deckers, J., Thijs, L, and Van Humeeck, J., "Part and material properties in selective laser melting of metals," the 16th Intl. Symp., on Electromachining, 2010, pp. 3 -14.

[40] Bartlett, J., Croom, B., Burdick, J., Henkel, D., and Li, X., "Revealing mechanisms of residual stress development in additive manufacturing via digital image correlation," J. Additive Manufacturing, Vol. 22, 2018, pp. 1 – 12.

[41] Bauereiss, A., Scharowsky, T., and Koerner, C., "Defect generation and propagation mechanism during additive manufacturing by selective beam melting," J. of Material Processing Technology, Vol. 214, 2014, pp. 2522 – 2528.

[42] Lewandowski, J. and Seifi, M., "Metal additive manufacturing: A review of Mechanical Properties," Annu. Rev. Mater. Res. Vol. 46, 2016, pp. 151 – 186.

[43] ISO/ASTM 52921-13 Standard Terminology for Additive Manufacturing - Coordinate Systems and Test Methodologies, International Organisation for Standardization, 2019.

[44] Cheng, H., Lu, C., Liu, J., et al., "Synchrotron radiation X-ray powder diffraction techniques applied in hydrogen storage materials - A review," Progress in Natural Science: Materials International, Vol. 27, 2017, pp. 66 – 73.

[45] Brown, C. and Donmez, A., "Microstructure Analysis for Additive Manufacturing: A Review of Existing Standards," NIST Advanced Manufacturing Series 100-3, the National Institute of Standards and Technology, Gaithersburg, Maryland, 2016.

[46] ASTM International ASTM E112 - Standard Test Methods for Determining Average Grain Size (ASTM International, West Conshohocken, PA).

[47] ASTM International ASTM E930 - Standard Test Method for Estimating the Largest Grain Observed in a Metallographic Section (ALA Grain Size) (ASTM International, West Conshohocken, PA).

[48] ASTM International ASTM E1181 - Standard Test Methods for Characterizing Duplex Grain Sizes (ASTM International, West Conshohocken, PA).

[49] ASTM International ASTM E1382 - Standard Test Methods for Determining Average Grain Size Using Semiautomatic and Automatic Image Analysis (ASTM International, West Conshohocken, PA).

[50] ASTM International ASTM E2627 - Standard Practice for Determining average grain size using electron backscatter diffraction (EBSD) in fully recrystallized polycrystalline materials (ASTM International, West Conshohocken, PA).

[51] International Organization for Standardization ISO 643 - Steels — Micrographic determination of the apparent grain size (International Organization for Standardization, Geneva, Switzerland).

[52] International Organization for Standardization ISO 2624 - Copper and copper alloys — Estimation of average grain size (International Organization for Standardization, Geneva, Switzerland).

[53] International Organization for Standardization ISO 4499-1 - Hardmetals — Metallographic determination of microstructure — Part 1: Photomicrographs and description (International Organization for Standardization, Geneva, Switzerland).

[54] International Organization for Standardization ISO 14250 - Steel — Metallographic characterization of duplex grain size and distributions (International Organization for Standardization, Geneva, Switzerland).

[55] ASTM International ASTM E543 - Standard Specification for Agencies Performing Nondestructive Testing (ASTM International, West Conshohocken, PA).

[56] ASTM International ASTM E45 - Standard Test Methods for Determining the Inclusion Content of Steel (ASTM International, West Conshohocken, PA).

[57] ASTM International ASTM E2142 - Standard Test Methods for Rating and Classifying Inclusions in Steel Using the Scanning Electron Microscope (ASTM International, West Conshohocken, PA).

[58] ASTM International ASTM E82/E82M - Standard Test Method for Determining the Orientation of a Metal Crystal (ASTM International, West Conshohocken, PA).

[59] Lane, B., Moylan, S., Yeung, H., Neira, J., and Chavez-Chao, J., "Quasi-Static Position Calibration of the Galvanometer Scanner on the Additive Manufacturing Metrology Testbed," NIST Technical Note 2099, Gaithersburg, MD 20899, 2020.

[60] Besl, P. and McKay, N., "Method for registration of 3-d shapes. In *Sensor fusion IV: control paradigms and data structures*," International Society for Optics and Photonics, Vol 1611, 586–606. 1992.

[61] Lane, B. and Yeung, H., "Process Monitoring Dataset from the Additive Manufacturing Metrology Testbed (AMMT): Three-Dimensional Scan Strategies", Journal of Research, National Institute of Standards and Technology, Gaithersburg, MD, 2019, https://doi.org/10.6028/jres.124.033.

[62] Richard Hartley and Andrew Zisserman (2003). *Multiple View Geometry in computer vision*. Cambridge University Press.

[63] Zhang, Z., A Flexible New Technique for Camera Calibration, 1998, https://www.microsoft.com/en-us/research/wp-content/uploads/2016/02/tr98-71.pdf

[64] R. Storn and K. Price, "Differential Evolution – A Simple and Efficient Heuristic for Global Optimization over Continuous Spaces," J. Glob. Optim., vol. 11, pp. 341–359, 1997, doi: https://doi.org/10.1023/A:1008202821328.

[65] Sundar, V., Snow, Z., Keist, J. *et al.* Flaw Identification in Additively Manufactured Parts Using X-ray Computed Tomography and Destructive Serial Sectioning. *J. of Materi Eng and Perform* **30**, 4958–4964 (2021). https://doi.org/10.1007/s11665-021-05567-w

[66] ASTM International ASTM E3 - Standard Guide for Preparation of Metallographic Specimens (ASTM International, West Conshohocken, PA).

[67] ASTM International ASTM E407 - Standard Practice for Microetching Metals and Alloys (ASTM International, West Conshohocken, PA).

[68] International Organization for Standardization ISO 4499-1 - Hardmetals — Metallographic determination of microstructure — Part 1: Photomicrographs and description (International Organization for Standardization, Geneva, Switzerland).